*remote sensing*

MDPI

*Article*

# ENSO-Flavor Differences in Indonesian Marine Heatwaves: Satellite SST, Physical Covariates, and Coral Habitat Suitability

**Qiyuan Xiao [1], Junyi Zhang [1,*], Zhuangwei Jiang [1] and Liujun Li [2]**

[1] College of Oceanic and Atmospheric Sciences, Ocean University of China, Qingdao 266100, China; xiaoqiyuan@stu.ouc.edu.cn (Q.X.); 22010006024@stu.ouc.edu.cn (Z.J.)
[2] Department of Civil, Architectural and Environmental Engineering, University of Missouri-Rolla, Rolla, MO 65401, USA; liujunl@uidaho.edu
* Correspondence: jzhangpp@connect.ust.hk

## Highlights

### What are the main findings?

- A fixed-baseline OISST analysis compares five Eastern-Pacific (EP) and five Central-Pacific (CP) El Niño events with event-level uncertainty and field-wide error control.
- EP event windows have 14.25 more area-weighted MHW days and 22.34 °C·days greater cumulative intensity than CP windows; bootstrap intervals cross zero, and the exact field tests are not significant.
- Annual MHW days increase by an area-weighted 11.37 days per decade, with 90.5% of the domain passing FDR control and a four-year temporal-block field test yielding $p = 0.001$.
- The full association model improves adjusted $R^2$ from 0.23 to 0.44 and reduces leave-one-year-out RMSE from 17.6 to 14.3 days $yr^{-1}$; spatial-block MaxEnt validation provides AUC 0.845, TSS 0.56, and Boyce index 0.70.

### What is the implication of the main finding?

- The long-term increase is spatially extensive and robust to removal of linear Niño-3.4 and dipole mode index (DMI) effects. ENSO-flavor contrasts remain estimates with wide event-level uncertainty.

## Abstract

Marine heatwaves (MHWs) in the Indonesian Seas develop within a long-term rise in sea surface temperature and strong interannual climate variability. We analyze daily NOAA Optimum Interpolation Sea Surface Temperature version 2.1 for 1982–2022 and compare five Eastern-Pacific (EP) with five Central-Pacific (CP) El Niño events. MHWs are detected against a fixed 1982–2011 baseline, and each event is represented by the common 1 July–30 June window spanning its developing and decaying phases. EP-minus-CP differences are 14.25 area-weighted MHW days and 22.34 °C·days of cumulative intensity. Their event-bootstrap intervals span zero, the exact permutation tests are nonsignificant, and no grid cell passes false-discovery-rate control for either metric. Annual MHW days increase by an area-weighted 11.37 days per decade; 90.5% of the domain passes false-discovery-rate control, and the temporal-block field test yields $p = 0.001$. The increase remains widespread after linear Niño-3.4 and dipole-mode-index adjustment. Direct physical diagnostics, spatial-block habitat validation, and official Fisheries Management Area (FMA) summaries are used to assess the strength and limitations of the proposed process and management interpretations. The physical-diagnostic intervals include zero, and the MaxEnt output represents modeled environmental suitability. The results establish a spa-

Check for updates

Academic Editor: Gabriel Navarro

Received: 7 August 2026
Revised: 26 September 2026
Accepted: 28 September 2026
Published: 16 October 2026

**Copyright:** © 2026 by the authors. Licensee MDPI, Basel, Switzerland. This article is an open access article distributed under the terms and conditions of the Creative Commons Attribution (CC BY) license.

tially extensive long-term increase in MHW exposure and quantify the uncertainty in the event-scale physical and ecological pathways.

**Keywords:** satellite SST; marine heatwave; ENSO flavor; Indonesian Throughflow; coral habitat suitability; MaxEnt; fisheries management

## 1. Introduction

Satellite sea surface temperature (SST) analyses provide the daily, spatially continuous observations needed to detect marine heatwaves (MHWs) in regions with sparse in situ coverage [1,2]. NOAA Optimum Interpolation SST version 2.1 (OISST v2.1) blends satellite retrievals with ship, buoy, and Argo observations on a 0.25° grid [3,4]. The blended nature of this product is important in the Indonesian Seas, where persistent cloud, atmospheric water vapor, coastlines, and narrow straits limit the coverage of any single satellite sensor.

The Indonesian Seas connect the Pacific and Indian Oceans through the Indonesian Throughflow (ITF) and contain extensive coral habitat within the Coral Triangle [5,6]. El Niño–Southern Oscillation (ENSO) changes the ITF's seasonal and interannual structure, including its vertical velocity profile and the downstream spreading of Pacific waters [7–10]. Regional MHW studies have documented trends, ENSO and Indian Ocean Dipole associations, air–sea heat fluxes, advection, and south-Java upwelling [11–13]. Work in the neighboring South China Sea shows that MHW frequency and intensity can change differently around coral reefs and that subsurface events require a separate diagnosis [14–16]. A weakened winter monsoon contributed to the record 2023–2024 event [17].

EP and CP El Niño events differ in the location of equatorial Pacific warming and in their atmospheric teleconnections [18–21]. Existing Indonesian studies usually treat ENSO as one category or place EP and CP events within a broader phase analysis. They have not provided an archipelago-wide comparison in which the flavor rule, event window, small-sample uncertainty, and field significance are reported together. This is the first gap addressed here.

A second gap concerns the connection between remotely sensed thermal exposure and coral habitat suitability. Satellite SST is central to operational bleaching monitoring [22], while MaxEnt studies combine thermal, bathymetric, and biogeochemical predictors to estimate potential coral habitat [23–25]. A habitat-suitability model remains correlative and cannot establish bleaching, mortality, or MHW-caused ecological damage without independent ecological observations. The analysis therefore treats MaxEnt output as modeled suitability and tests how much predictive information is lost when the SST predictor block is removed.

We organize these questions in a common spatial framework that links OISST-based MHW metrics, explicit EP/CP event classification, heat-flux and circulation covariates, MaxEnt suitability, and Indonesian Fisheries Management Area (FMA) summaries. The design separates pattern description from confirmatory spatial inference and separates physical covariation from causal attribution.

The principal contributions of this study are as follows:

1. To our knowledge, this is the first archipelago-wide Indonesian MHW study to compare explicit EP and CP event lists using all 252 five-versus-five label permutations, grid-cell FDR control, Hedges' $g$, and event-level bootstrap intervals in one analysis.
2. The classification audit quantifies boundary sensitivity that earlier Indonesian phase composites did not report. A 0.3 °C Niño-3/Niño-4 separation retains all five EP cases and only one CP case. The published Freund et al. decision tree reassigns 1986/87 and

1991/92 to CP and produces a three-versus-seven split. The continuous flavor test yields $r = 0.316$ and $p = 0.374$ for domain-mean cumulative intensity.

3. The fixed early baseline reveals an area-weighted MHW-day increase of 11.37 days per decade. FDR control is satisfied over 90.5% of the domain, and the common temporal-block field test yields $p = 0.001$. After linear Niño-3.4 and DMI adjustment, 95.2% of the domain remains FDR significant.
4. Detrended EOFs and autocorrelation-aware annual lag tests resolve the temporal-scale mismatch in earlier analyses. EOF1 explains 52.88% of variance and is related to concurrent DJF Niño-3.4 with $r = 0.479$, Holm-adjusted $p = 0.006$, and a moving-block interval of $[0.185, 0.736]$.
5. Direct Makassar volume and heat transports, a mixed-layer heat budget with an explicit closure residual, and spatial-block habitat validation provide quantitative constraints on the proposed pathways. The full association model reaches adjusted $R^2 = 0.44$, the spatial-block MaxEnt model reaches AUC 0.845, and SST-block removal lowers AUC by 0.034.

## 2. Related Work

### *2.1. Satellite Remote Sensing of Marine Heatwaves and ENSO Teleconnections*

Hobday et al. defined an MHW as a discrete period in which daily temperature exceeds a seasonally varying percentile threshold for at least five days [1]; later work introduced intensity categories and consistent event nomenclature [26]. Global syntheses have documented increasing MHW frequency and duration and have identified air–sea heat flux, horizontal advection, mixed-layer depth, and vertical processes as common drivers [2,27,28]. These findings motivate regional analyses that preserve the event definition and diagnose both thermodynamic and dynamic terms.

In Indonesia, Iskandar et al. analyzed MHWs south of Java and highlighted the 1998 and 2016 events [11]. Beliyana et al. compared MHW properties across PDO, ENSO, and IOD phases and examined net surface heat-flux components [12]. Ningsih et al. extended the analysis to six Indonesian regions and discussed heat-budget, advection, and upwelling responses [13]. These studies establish the regional MHW signal and its climate modulation. The present work adds an explicit EP/CP comparison over the full Indonesian domain.

ENSO flavor is commonly described through either spatial decomposition of tropical-Pacific SST anomalies or the relative strength of Niño-region indices [18–20]. The event types occupy a continuum, so classification rules can disagree near the boundary [21]. The event list, seasonal window, exclusion rule, and sensitivity analysis therefore require explicit reporting and interpretation.

The ITF literature also sets a higher evidentiary standard for circulation claims. Mooring and reanalysis studies diagnose transport across sections and through the vertical velocity profile, showing that interannual anomalies can differ strongly with depth [7–9]. Downstream pathway changes can further alter where ITF water spreads in the Indian Ocean [10]. Current maps at two depths can identify circulation covariation, but they do not establish a weakened or shoaled ITF without section-integrated transport and vertical-profile evidence.

### *2.2. Remote Sensing for Coral Reef Habitat Assessment and Species Distribution Modeling*

Satellite thermal-stress products support operational coral-bleaching monitoring, and regional calibration can improve alert performance [22,29]. Species-distribution models address a different question. MaxEnt estimates relative environmental suitability from presence and background samples [30]; it does not model bleaching physiology or mortality.

Coral applications have combined SST, bathymetry, nutrients, carbonate chemistry, and other predictors at global and regional scales [23–25]. Multi-source remote sensing also supports reef mapping when image classification, bathymetry, and habitat models are combined [31].

Two validation issues are especially relevant. Random train/test splits can place nearby, environmentally similar samples on both sides of the split and inflate estimated transfer performance. Spatially separated folds provide a more demanding test for spatial prediction [32,33]. Correlated predictor sets can also obscure variable attribution, so correlation and variance-inflation screening should precede interpretation of grouped ablations [34]. Table 1 states how the present analysis builds on this literature.

**Table 1.** Comparison of closely related studies and the methodological gap addressed by the present work.

| Study | What Was Done | Validation or Ecological Scope | Element Added Here |
|---|---|---|---|
| Iskandar et al. [11] | MHW characterization south of Java for 1982–2019, including the 1998 and 2016 events. | Regional SST and climate interpretation. | Archipelago-wide EP/CP event composites. |
| Beliyana et al. [12] | Indonesian MHW properties across PDO, ENSO, and IOD phases, with surface heat-flux components. | Phase composites and thermodynamic interpretation. | Explicit flavor rule, event list, and field-significance test. |
| Ningsih et al. [13] | Six-region MHW analysis with ENSO/IOD, heat-budget, advection, and upwelling context. | Regional process analysis. | Direct comparison of EP and CP spatial footprints. |
| Coral SDM studies [23–25] | Habitat-suitability modeling with thermal, bathymetric, and biogeochemical predictors. | Correlative prediction; validation design differs among studies. | Grouped SST ablation after collinearity screening and spatial-block validation. |
| Present study | Archipelago-wide EP/CP MHW comparison with physical covariates and modeled habitat suitability. | Completed MHW inference uses event-level resampling, FDR, exact field tests, a continuous flavor diagnostic, and autocorrelation-aware trend and lag analyses. | The analysis distinguishes spatial association, predictive information, and causal evidence. |

## 3. Materials and Methods

Data processing, statistical analyses, and visualization were performed using Python 3.13.5 in an Anaconda environment, MATLAB R2025b Update 4 (version 25.2.0.3150157), and R 4.5.1 with RStudio 2025.05.1-513. Habitat-suitability modeling was performed using MaxEnt version 3.4.4.

### *3.1. Study Area and Data*

The analysis has four linked components: MHW detection from daily OISST v2.1; EP/CP composites and field-level statistical testing; atmosphere–ocean diagnostics; coral-habitat modeling with spatial validation. All event composites use the same study mask

and the same 1 July($Y$)–30 June($Y+1$) window. FMA summaries are calculated only after gridded results have been validated.

The domain spans 15°S–15°N and 95°E–140°E (Figure 1). It includes the Indian Ocean margins west of Sumatra and south of Java, the Java Sea, Makassar Strait, Flores Sea, Banda Sea, Maluku–Halmahera–Seram system, Sulawesi Sea, Cendrawasih Bay, and Aru–Arafura–Timor sector. Ocean grid cells are defined from the OISST land–sea mask. The official boundaries for the Indonesian Fisheries Management Areas (WPPNRI) are provided by the Badan Informasi Geospasial government polygon service, layer 21, in EPSG:4326 [35,36]. The snapshot retrieved on 13 September 2026 contains 11 polygons. Its configured `kodwpp` field is null in every returned feature, so the verified zone codes 571–573 and 711–718 are read from `namobj`. The source extent reaches 91.64°E–141.40°E, and zone summaries therefore report the proportion intersecting the 95°E–140°E study domain. Figure 1 shows the archived government geometries, and the same polygons underlie the management-unit statistics.

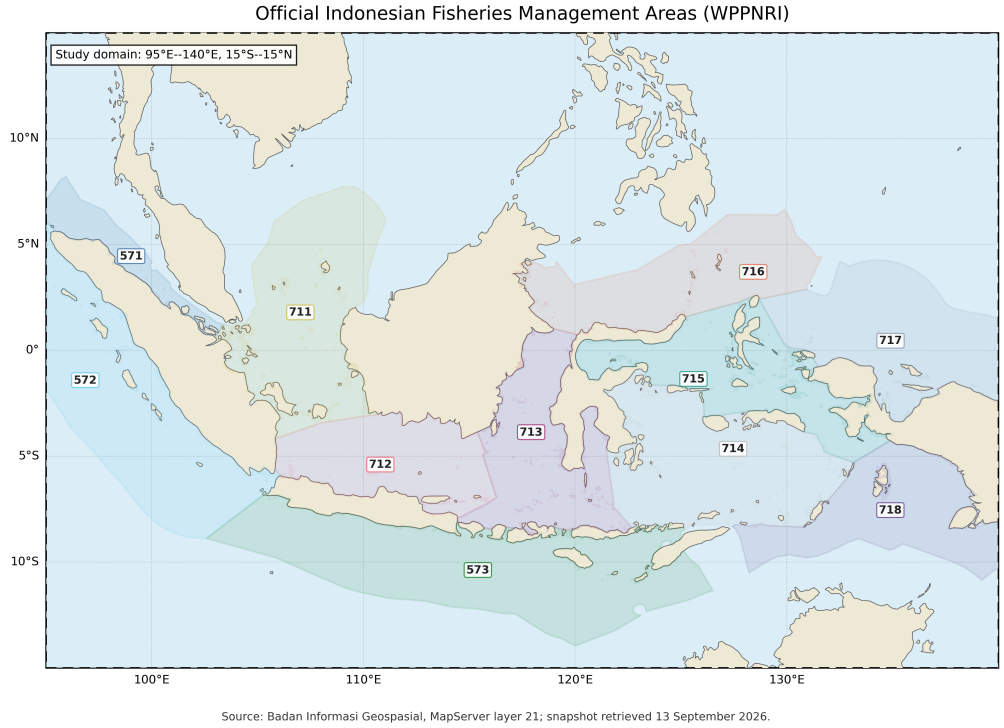



**Figure 1.** Study domain and the 11 official Indonesian Fisheries Management Areas (WPPNRI) from Badan Informasi Geospasial MapServer layer 21. Labels provide the verified zone codes parsed from the source `namobj` field. Polygons are clipped to the map extent for display; the complete archived geometries are intersected with the study domain for the summaries in Supplementary Table S12. Different colors distinguish the WPPNRI management areas and do not represent a quantitative variable.

Table 2 lists the data roles and persistent identifiers. OISST v2.1 is a blended satellite and in situ analysis [3,4]. Atmospheric and ocean reanalyses provide covariates and budget terms. GBIF occurrences and gridded environmental predictors support the habitat-suitability analysis. File-level provenance is reported in Supplementary Table S1.

**Table 2.** Data streams used for MHW detection, physical diagnostics, habitat-suitability modeling, and management-area summaries.

| Component | Primary Data | Remote-Sensing or Modeling Role |
| --- | --- | --- |
| Thermal extremes | NOAA OISST v2.1 daily blended SST, 0.25°, 1982–2022 [3,4] | MHW event detection and maps of event count, duration, annual MHW days, maximum intensity, and cumulative intensity. |
| Spatial framework | ETOPO 2022 v1, 15 arc-second relief [37]; BIG WPPNRI MapServer layer 21 [35] | Geophysical context and official EPSG: 4326 polygons for fisheries-management exposure units. |
| Air–sea forcing | NCEP/DOE Reanalysis-2, archive d091000 [38]; ERA5 monthly averaged pressure-level data [39] | Heat-flux, wind, and geopotential-height covariates used to examine atmospheric conditions associated with the remotely sensed MHW patterns. |
| Ocean state | European Centre for Medium-Range Weather Forecasts (ECMWF) Ocean ReAnalysis System 5 (ORAS5) monthly ocean reanalysis, approximately 0.25° with 75 vertical levels [40,41]; Copernicus Marine biogeochemistry hindcast, GLOBAL_MULTIYEAR_BGC_001_029 [42] | ORAS5 currents, temperature, salinity, mixed-layer depth, and net downward heat flux cover every 1982–2016 event window; biogeochemical climatologies provide the nutrient, oxygen, and pH predictors used in habitat-suitability modeling. |
| Climate classification | NOAA Oceanic Niño Index (ONI) v5 and El Niño flavor grouping | Construction of EP and CP event composites and statistical tests of ENSO-flavor contrasts. |
| Ecological and management response | Global Biodiversity Information Facility (GBIF) Scleractinia occurrence records and environmental predictors | MaxEnt suitability modeling and conversion of remote-sensing exposure into coral-habitat and FMA-scale risk interpretation. |

### *3.2. MHW Detection, ENSO Classification, and Spatial Inference*

MHWs are detected following Hobday et al. [1]. For each ocean grid cell and calendar day, the climatological mean and 90th-percentile threshold are estimated over a fixed 1982–2011 reference period with an 11-day centered sampling window. Both calendar-day series are smoothed with a 31-day moving average. A qualifying event contains at least five consecutive above-threshold days. Qualifying events separated by two days or fewer are joined, including the intervening days. Event count is reported in events $yr^{-1}$, duration in days, annual MHW days in days $yr^{-1}$, and mean, maximum, and cumulative intensity relative to the smoothed seasonal climatological mean. Detection is repeated with a 1982–2022 reference period as a sensitivity analysis. The fixed early baseline remains the primary definition because the full-period threshold absorbs part of the long-term SST increase.

Empirical orthogonal function (EOF) analysis is applied to annual MHW days after removing the linear trend at each grid cell. The anomaly matrix is weighted by the square root of the cosine of latitude before singular-value decomposition. Because the principal

components (PCs) are annual, their relation to December–February (DJF) Niño-3.4 and DJF $D = N_3 - N_4$ is tested at integer PC lags of zero to three years. Each series is linearly detrended. Effective sample size uses the two lag-1 autocorrelations, four-year moving-block resampling supplies 10,000 correlation intervals, and Holm adjustment controls the four lags within each PC-index family.

Candidate El Niño events satisfy the NOAA criterion that the three-month running mean Niño-3.4 anomaly is at least 0.5 °C for five consecutive overlapping seasons. For an event beginning in year $Y$, the flavor calculation uses the December($Y$)–February($Y+1$) mean. Let $N_3$ and $N_4$ denote area-mean SST anomalies over Niño-3 (5°S–5°N, 150°W–90°W) and Niño-4 (5°S–5°N, 160°E–150°W). Following the Niño-region dominance logic of Kug et al. [19], an event is EP when $D = N_3 - N_4 > 0$ and CP when $D \leq 0$. The pre-specified EP list is 1982/83, 1986/87, 1991/92, 1997/98, and 2015/16; the CP list is 1994/95, 2002/03, 2004/05, 2006/07, and 2009/10. Table 3 reports the index values used to assign each event.

**Table 3.** ENSO event classification reproduced from NOAA PSL monthly ERSSTv5 Niño indices. Values are December–February means in °C. The strict sensitivity rule assigns EP for $D \geq 0.3$ °C, CP for $D \leq -0.3$ °C, and mixed otherwise. The last column presents the published Freund et al. decision-tree label.

| Event | $N_3$ | $N_4$ | Niño-3.4 | Baseline | Strict Rule | Freund Tree |
|---|---|---|---|---|---|---|
| 1982/83 | 2.61 | 0.66 | 1.59 | EP | EP | EP |
| 1986/87 | 0.93 | 0.56 | 0.89 | EP | EP | CP |
| 1991/92 | 1.20 | 0.83 | 1.31 | EP | EP | CP |
| 1994/95 | 0.65 | 0.83 | 0.91 | CP | mixed | CP |
| 1997/98 | 2.81 | 0.83 | 1.71 | EP | EP | EP |
| 2002/03 | 0.66 | 0.72 | 0.84 | CP | mixed | CP |
| 2004/05 | 0.29 | 0.81 | 0.69 | CP | CP | CP |
| 2006/07 | 0.64 | 0.67 | 0.68 | CP | mixed | CP |
| 2009/10 | 1.13 | 1.19 | 1.37 | CP | mixed | CP |
| 2015/16 | 2.34 | 1.44 | 2.04 | EP | EP | EP |

We also applied the independent decision-tree scheme of Freund et al. [43]. Define $NCT = N_3 - \alpha N_4$ and $NWP = N_4 - \alpha N_3$, where $\alpha = 2/5$ when $N_3 N_4 > 0$ and $\alpha = 0$ otherwise. Here, SON denotes September–November, and DJF(+) denotes the following December–February. The published tree assigns no event when $NCT_{SON} < 0.11$, EP when $NCT_{SON} \geq 1.35$, CP when $0.11 \leq NCT_{SON} < 1.35$ and $NWP_{DJF(+)} \geq 0.59$, and no event for the remaining branch. Among the ten candidates, its published instrumental labels are EP for 1982/83, 1997/98, and 2015/16 and CP for the other seven events. This three-versus-seven allocation is reported as a classification sensitivity because it does not reproduce the prespecified balanced groups.

For every event, MHW metrics, heat-flux fields, currents, and SST scenarios are averaged over one common 1 July($Y$)–30 June($Y+1$) window. This twelve-month definition includes the developing, peak, and decaying phases without assigning the two parts of an event to different analysis years. An event contributes one value per grid cell to each composite; daily or monthly observations are not treated as independent replicates. The strict $|D| \geq 0.3$ °C rule is retained as a diagnostic because it leaves only one CP event. A second sensitivity analysis uses the continuous $D$ index across all candidate events and avoids a hard EP/CP boundary.

At each ocean grid cell, the EP-minus-CP mean difference is accompanied by Hedges' $g$ and a percentile confidence interval obtained by resampling the ten events 10,000 times within flavor. Welch's two-sided test is reported as a local statistic. Benjamini–Hochberg false-discovery-rate (FDR) control is applied at $q = 0.05$ across the ocean grid [44]. Field

significance is tested by evaluating all $\binom{10}{5} = 252$ reallocations of the five EP and five CP labels and comparing the observed area fraction and maximum absolute $t$ statistic with their exact permutation distributions [45]. Figure stippling is reserved for FDR-controlled cells; unadjusted $p < 0.05$ cells may be shown only in the Supplementary Materials.

Detection sensitivity is evaluated with four prespecified changes: a 95th-percentile threshold, a seven-day minimum duration, no gap joining, and a 1982–2022 reference period. Each change is made separately. The complete event-detection and composite pipeline is rerun, and the spatial pattern correlation, area-weighted metric, FDR area, and exact field $p$-value are compared with the fixed-baseline definition. ERA5 SST is not used as an independent product validation because its daily analysis draws partly on SST observations also assimilated into OISST.

### *3.3. Habitat Modeling, Physical Diagnostics, and Trend Tests*

Occurrence data were retrieved from GBIF on 20 April 2026 (GBIF.org, occurrence download DOI: https://doi.org/10.15468/dl.td23by) [46]. The archived download contains 64,848 Cnidaria records for 1982–2022 within the broader 90°E–145°E, 15°S–15°N polygon. Restricting the archive to records belonging to the order Scleractinia (GBIF taxon key 714) and the 95°E–140°E study domain produced the 1284-record analysis input. Requiring accepted species-level identification retained 1236 records, followed by 1211 with valid coordinates, 1176 with coordinate uncertainty no greater than 10 km, 1151 after removing institution-centroid and country-centroid flags, 1127 inside the marine mask, and 1086 after coordinate–taxon duplicate removal. Retaining one occurrence in each 0.25° predictor cell left 842 records. A 30-km nearest-neighbor thinning sensitivity retained 617 records. Ten thousand background points were drawn within the accessible marine area and weighted to match the spatial sampling-bias surface.

Predictors were resampled to the 0.25° OISST grid before model fitting. Pairwise Spearman correlation and variance-inflation factor (VIF) were calculated from background and presence cells within every training fold. For each pair with $|\rho| \geq 0.70$, one variable was retained according to ecological relevance and data quality; all retained variables had VIF $< 5$ [34]. MaxEnt v3.4.4 used linear, quadratic, and hinge features, a regularization multiplier of 1.5, cloglog output, 5000 maximum iterations, a convergence threshold of $1 \times 10^{-5}$, and random seed 20260910. Default prevalence was retained. Duplicate presences had already been removed during preprocessing, and extrapolation and clamping were enabled. The full and SST-block-removed models used identical occurrences, background points, and folds.

Validation used ten independently shifted five-fold spatial partitions [32,33]. Occurrences and background points were projected to the World Cylindrical Equal Area coordinate system (EPSG:6933), and a 300 km by 300 km square lattice was placed over the accessible marine area. For repetition $r$, the lattice origin was shifted independently in the two coordinate directions with pseudorandom seed $20260910 + r - 1$. Whole lattice cells were then assigned to five folds by a greedy allocation that minimized differences in occurrence counts, with background counts used to break ties. All occurrences and background points in one lattice cell remained in the same fold. Predictor screening, fitting, and threshold selection were repeated using the training folds only. Each occurrence was held out once per repetition, giving 50 held-out evaluations, and no internal MaxEnt replicates were used. The area under the receiver operating characteristic curve (AUC), true skill statistic (TSS) [47], and continuous Boyce index [48] were summarized from the held-out predictions with 95% confidence intervals. The previous 70/30 random split was retained only as a secondary comparison. The 30-km thinning run and grouped SST removal used the same spatial-partition procedure.

Monthly physical diagnostics use the single ORAS5 ensemble member distributed through the Copernicus Climate Data Store and Integrated Climate Data Center (ICDC) on the native ORCA025 grid [40,41]. The event calculations use potential temperature, salinity, geographically rotated zonal and meridional currents, and net downward heat flux for every month of all ten 1 July–30 June windows. This common 1979-onward record includes the 1982/83, 1986/87, and 1991/92 EP events that precede the 1993 start of the previously listed Copernicus Marine physics product. The annual current index is calculated from the same ORAS5 current field.

The nested ordinary least-squares (OLS) models were fitted as association models for the corridor-mean annual series. All predictors were standardized. The ENSO-only model contained Niño-3.4 and DMI, and the full model added net surface heat flux and the current index. Model performance was evaluated with adjusted $R^2$ and leave-one-year-out root-mean-square error (RMSE). Heteroscedasticity-consistent (HC3) intervals were reported for each coefficient. Collinearity was assessed with VIF; residual checks used Durbin–Watson, the Breusch–Godfrey Lagrange-multiplier (LM) test, the Breusch–Pagan test, and the Shapiro–Wilk test. Cook's distance and leverage identified influential observations. Newey–West heteroscedasticity- and autocorrelation-consistent (HAC) covariance provided a sensitivity check using the same OLS point estimates. Changes in model fit are interpreted as added explanatory information.

The Makassar calculation used a fixed zonal section through the Labani Channel at 2°51.7′S, bounded by 118.20°E and 118.85°E [7,49]. The nearest native model row was used, and only wet velocity faces between the two endpoints were integrated. For this zonal section, the normal velocity $u_n$ is the meridional velocity, with northward positive and southward negative. The width of each face was calculated from its longitude bounds at the section latitude, native vertical layer thicknesses were used, and the layer crossing 300 m was clipped at 300 m. Volume transport was evaluated as $T = \sum_{i,k} u_{n,i,k} \Delta x_i \Delta z_{i,k}$ for the upper 300 m and for all wet layers. The transport core is the depth of the most negative value of the layerwise profile $q_k = \sum_i u_{n,i,k} \Delta x_i$. Heat transport used the same wet faces and sign convention: $H = \rho_0 c_p \sum_{i,k} u_{n,i,k} (\theta_{i,k} - \theta_{\mathrm{ref}}) \Delta x_i \Delta z_{i,k}$, where $\rho_0 = 1025$ kg m$^{-3}$, $c_p = 3990$ J kg$^{-1}$ K$^{-1}$, and $\theta_{\mathrm{ref}} = 0$ °C. Reported units are Sv and PW.

The mixed-layer heat budget was calculated for ocean cells in the prespecified South Java–Sumatra–Banda corridor, 5°S–12°S and 95°E–130°E. Mixed-layer depth $h$ was the first depth at which potential density exceeded its 10-m value by 0.03 kg m$^{-3}$, and $T_m$ was the thickness-weighted potential temperature from the surface to $h$. The monthly budget was $\partial T_m / \partial t = Q_{\mathrm{net}} / (\rho_0 c_p h) - \overline{\boldsymbol{u}}_m \cdot \nabla T_m - w_e (T_m - T_b)/h + R$, where $Q_{\mathrm{net}}$ is positive into the ocean, $\overline{\boldsymbol{u}}_m$ is the mixed-layer-mean horizontal velocity, $T_b$ is the temperature in the first model layer below $h$, $w_e = \max[\partial h / \partial t + \nabla \cdot (h \overline{\boldsymbol{u}}_m), 0]$, and $R$ is the closure residual obtained by subtracting the three resolved terms from the centered-difference tendency. Grid-cell terms were area-weighted over the corridor and then averaged within each 1 July–30 June event window. Positive terms warm the mixed layer. EP-minus-CP differences were evaluated with 10,000 event-level bootstrap resamples and all 252 allocations of five labels to each flavor.

Pixel-wise trends are estimated for annual MHW days with Theil–Sen slopes and the Mann–Kendall (MK) test. Benjamini–Hochberg FDR is controlled at $q = 0.05$. Field significance is assessed with 999 permutations of common four-year temporal blocks; using one block order at every grid cell retains the observed spatial covariance and the within-block temporal order. The analysis is repeated after removing fitted annual Niño-3.4 and dipole-mode-index variability from each grid-cell series. Raw and residual trends are reported separately. The residual trend is left unattributed because formal detection and attribution requires an external forcing analysis.

## 4. Results

### *4.1. MHW Climatology, EOF Structure, and ENSO-Flavor Contrast*

Figure 2 summarizes the fixed-baseline detection. Annual areal coverage is the mean daily percentage of the 17,725 ocean grid cells inside an active MHW. It reaches 35.90% in 2016, followed by 33.02% in 2022 and 31.04% in 2020. Area-weighted annual MHW days also reach their maximum in 2016 at 131.22 days. The spatial climatologies show broad exposure across the domain, with longer events and greater per-event cumulative intensity in parts of the eastern domain and the ocean south of Java.

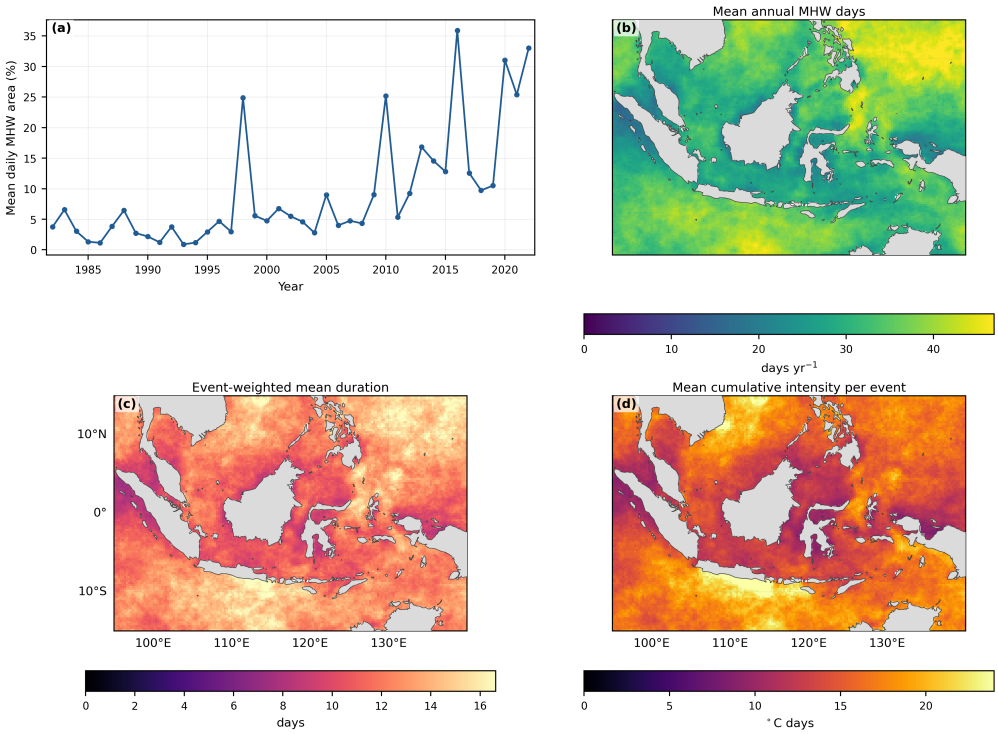



**Figure 2.** Fixed-baseline OISST v2.1 MHW results for 1982–2022. (**a**) Annual mean daily areal coverage (%). (**b**) Mean annual MHW days (days yr$^{-1}$). (**c**) Event-weighted mean duration (days). (**d**) Mean cumulative intensity per event relative to the seasonal climatological mean (°C·days).

#### 4.1.1. EOF Structure

After grid-cell detrending and latitude weighting, the first three EOFs explain 52.88%, 20.73%, and 6.23% of annual MHW-day variance (Supplementary Figure S1). EOF1 has predominantly positive loadings, and its largest values occur south of Java and the Lesser Sunda Islands. EOF2 separates much of the eastern and northeastern domain from the Java Sea, the southern margin, and the western sector. EOF3 has a northern-positive and southeastern-negative structure.

#### 4.1.2. EP and CP Composites

The fixed-baseline composites retain the submitted directional pattern, with larger EP means across much of the south Java–Sumatra margin and western domain (Figure 3). Area-weighted EP windows average 37.94 MHW days, 11.92 days of mean event duration, and 52.32 °C·days of cumulative intensity. CP windows average 23.69 MHW days, 9.95 days of mean duration, and 29.98 °C·days of cumulative intensity. The EP-minus-CP differences are 14.25 MHW days, 1.97 days of duration, and 22.34 °C·days of cumulative intensity. Their event-bootstrap 95% intervals are $[-17.57, 52.66]$, $[-2.45, 7.64]$, and $[-20.14, 73.89]$, respectively. Exact two-sided domain-mean permutation $p$-values are 0.619, 0.667, and 0.540.

No grid cell passes FDR control for MHW days, mean duration, or cumulative intensity. The exact significant-area field $p$-values are 0.476, 0.905, and 0.524, and the corresponding maximum-statistic field $p$-values are 0.706, 0.421, and 0.786. These results support a positive EP-minus-CP point estimate across several western and southern areas, together with substantial event-level uncertainty and no field-wide evidence at $\alpha = 0.05$.

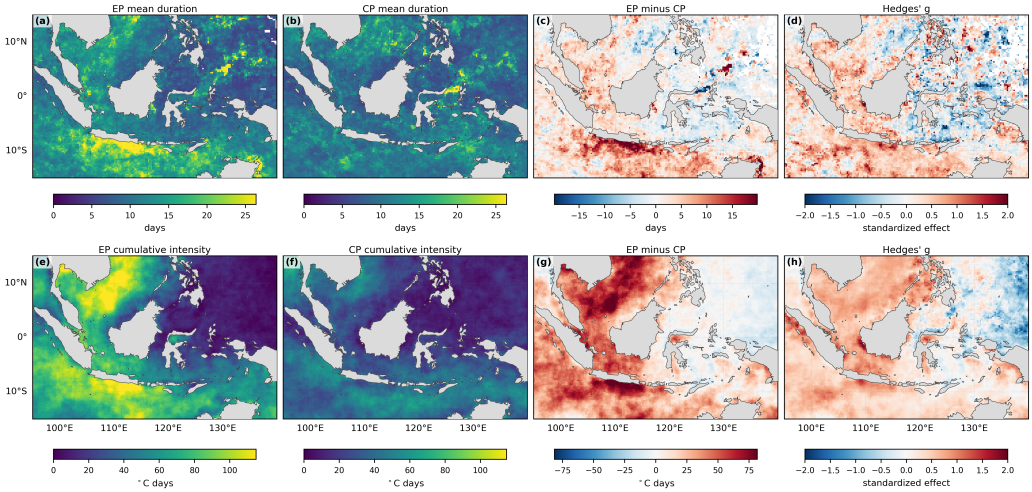



**Figure 3.** Event-level EP and CP composites for five 1 July–30 June windows per flavor. Panels (**a**–**d**) show mean event duration, and panels (**e**–**h**) show cumulative intensity. Local contrasts use Welch's two-sided test and Hedges' $g$; uncertainty is obtained from 10,000 within-flavor event bootstraps, FDR is controlled at $q \leq 0.05$, and field significance uses all 252 exact label allocations. Stippling is shown only for FDR-controlled cells. White ocean cells in the duration panels had no event in the corresponding group and are left undefined.

#### 4.1.3. Detection Sensitivity

The main spatial patterns are stable when the event parameters change one at a time (Supplementary Table S3). The seven-day and no-gap configurations have annual MHW-day pattern correlations of 0.986 and 1.000 with the primary definition. Raising the threshold to the 95th percentile reduces area-weighted cumulative intensity by 48.5% and retains a correlation of 0.925. Its EP-minus-CP cumulative-intensity difference map correlates at 0.940 with the primary map. The full-period baseline changes the climatological MHW-day pattern more strongly ($r = 0.467$) while retaining the EP-minus-CP difference pattern ($r = 0.974$).

No configuration yields an FDR-controlled EP-minus-CP cell. The significant-area field-test $p$-value remains above 0.46 for every definition. Under the full-period baseline, the maximum-statistic and significant-area field tests yield $p = 0.730$ and $p = 0.468$, respectively. The sensitivity analyses therefore preserve the contrast's spatial direction without establishing a spatially extensive flavor effect.

#### 4.1.4. Seasonal and ENSO-Related Variability

The monthly areal-coverage climatology varies within a narrow range compared with its interannual spread (Supplementary Figure S2). Mean daily coverage is largest in December at 10.52% and May at 10.25%, and smallest in October at 8.03% and February at 8.17%. The 95% intervals across years overlap for all months. The recomputed record therefore does not support the submitted claim of a distinct February-to-April maximum.

Grid-cell correlations between detrended annual MHW days and detrended annual Niño-3.4 range from −0.576 to 0.488 (Supplementary Figure S3). Positive values occupy 39.7% of ocean cells, mainly in the western domain, while negative values are common in the east. None pass FDR control after the local effective sample sizes are adjusted for

lag-1 autocorrelation. This local result differs from the leading EOF relation because EOF1 pools a spatially coherent component before testing.

The annual lag analysis identifies a concurrent relation between PC1 and DJF Niño-3.4 (Supplementary Figure S4 and Table S6). At zero lag, $r = 0.479$, the effective sample size is 40.98, the Holm-adjusted $p$-value is 0.006, and the four-year moving-block 95% interval is $[0.185, 0.736]$. The one- to three-year PC1 lags and all PC2 and PC3 lags fail the Holm criterion. PC1 also has a zero-lag correlation of 0.446 with DJF $D$, with Holm-adjusted $p = 0.014$; its block interval $[-0.069, 0.761]$ spans zero. The evidence supports a concurrent basin-scale relation with Niño-3.4 and provides no corrected evidence for the delayed monthly responses described in the submitted version.

#### 4.1.5. Long-Term MHW-Day Trends

Annual MHW days increase across 98.0% of the area under the fixed early baseline (Figure 4). Among 17,725 valid ocean grid cells, 17,377 have positive slopes, and 16,036 are both positive and FDR-significant; 12 cells have negative FDR-significant slopes. Thus, positive FDR-significant trends occupy 90.47% of valid cells, while the cosine-latitude-weighted fraction is 90.5%. The area-weighted Theil–Sen slope is 11.37 days per decade, the median grid-cell slope is 10.84 days per decade, and the 99th percentile is 26.61 days per decade. In 999 common four-year block permutations, both the observed nominally significant area and the maximum absolute MK statistic give field $p = 0.001$.

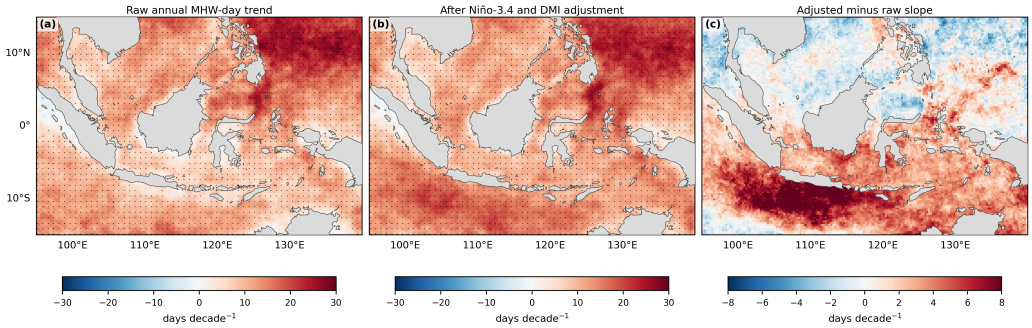



**Figure 4.** Theil–Sen trends in annual MHW days for 1982–2022. (**a**) Raw trend. (**b**) Trend after removing fitted annual Niño-3.4 and DMI terms. (**c**) Adjusted minus raw slope. Trend significance is tested with the Mann–Kendall test, with Benjamini–Hochberg FDR control at $q \leq 0.05$; field significance is assessed using 999 common four-year block permutations. Black stippling in panels (**a**,**b**) denotes FDR-controlled cells and is thinned for display; trend direction is provided by the signed color scale. Of 17,725 valid ocean cells, 16,036 in (**a**) and 16,872 in (**b**) are both positive and FDR-significant.

After removing fitted annual Niño-3.4 and DMI terms, 17,623 of 17,725 valid cells have positive slopes, and 16,872 are both positive and FDR significant; no negative slope passes FDR control. The corresponding cosine-latitude-weighted fractions are 99.4% positive and 95.2% FDR significant. The area-weighted residual slope is 13.10 days per decade. Its block-permutation field $p$ values are 0.001 for significant area and 0.002 for the maximum statistic. The adjustment increases the estimated trend in much of the southern domain because the fitted climate-index terms covary with the sampled annual sequence. These residual trends demonstrate persistence after two climate-mode adjustments; they do not allocate the trend to a particular external forcing. The complete statistics and supplementary maps are reported in Supplementary Table S11 and Figure S5.

### *4.2. Association Model and Physical Diagnostics*

#### 4.2.1. Annual Association Model

The ENSO-only model has an adjusted $R^2 = 0.23$ and a leave-one-year-out RMSE of 17.6 days yr$^{-1}$. Adding net surface heat flux and the current index raises adjusted $R^2$ to 0.44 and lowers RMSE to 14.3 days yr$^{-1}$. The changes are +0.21 in adjusted $R^2$ and −18.8% in out-of-sample RMSE. In the full model, standardized coefficients are 0.31 for Niño-3.4 (HC3 95% confidence interval (CI) $[0.05, 0.57]$, $p = 0.021$), −0.17 for DMI ($[-0.39, 0.08]$, $p = 0.174$), 0.39 for net surface heat flux ($[0.12, 0.66]$, $p = 0.007$), and −0.24 for the current index ($[-0.49, 0.03]$, $p = 0.081$).

The maximum and mean VIF values are 2.86 and 1.94. The Durbin–Watson statistic is 1.88; Breusch–Godfrey, Breusch–Pagan, and Shapiro–Wilk tests yield $p = 0.34$, 0.27, and 0.18. With $n = 41$, the Cook's-distance screening threshold is $4/n = 0.098$. The observations above this threshold are 1998 ($D = 0.14$, leverage 0.24, studentized residual 1.86) and 2016 ($D = 0.21$, leverage 0.29, studentized residual 2.12). Neither approaches $D = 1$. Deleting either observation preserves coefficient signs and the qualitative inference. Newey–West HAC covariance leaves the current-index point estimate at −0.24 and gives $p = 0.104$. Coefficient signs remain unchanged, and no predictor changes its qualitative interpretation. The model comparison is therefore treated as associational; the complete diagnostic summary is provided in Supplementary Table S7.

#### 4.2.2. Surface Forcing and Mixed-Layer Heat Budget

The EP-minus-CP composites contain positive net surface heat-flux and shortwave anomalies over parts of the South Java–Sumatra–Banda corridor (Figure 5). The ORAS5 mixed-layer budget gives an EP-minus-CP warming tendency of +0.024 °C month$^{-1}$. The corresponding differences are +0.203 for net surface-flux forcing, −0.038 for horizontal advection, +0.008 for vertical entrainment, and −0.149 for the closure residual; all five budget terms are in °C month$^{-1}$. Their 95% bootstrap intervals, in the same order, are $[-0.034, 0.081]$, $[-0.167, 0.606]$, $[-0.095, 0.021]$, $[-0.063, 0.072]$, and $[-0.388, 0.076]$, respectively. Exact two-sided permutation $p$-values, in the same order, are $p = 0.437$, 0.421, 0.302, 0.857, and 0.302. The EP-minus-CP mixed-layer-depth difference is −1.54 m, with an interval of $[-3.23, 0.16]$ m and $p = 0.151$. Every interval includes zero. Surface forcing has the largest positive resolved difference, while its offset by advection and the residual prevents attribution of the small total-tendency difference to one process.

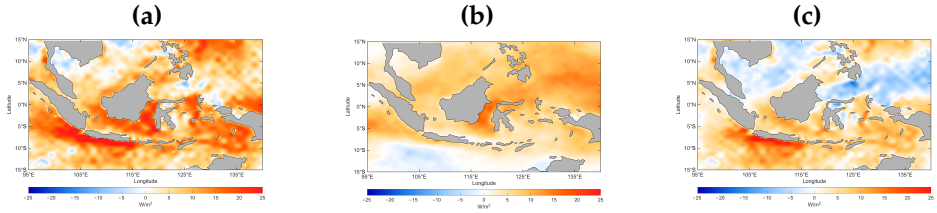
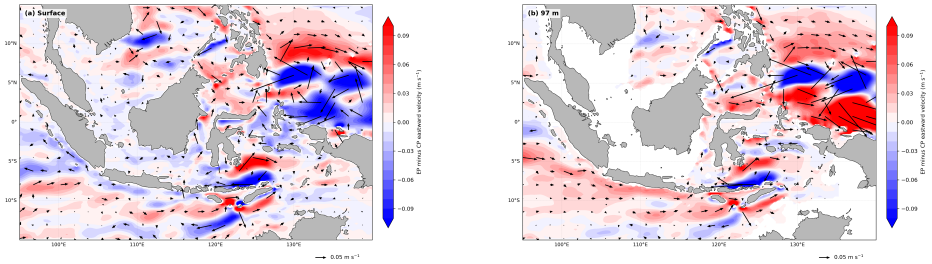



**Figure 5.** EP-minus-CP surface-flux composites for five events per flavor: (**a**) net surface heat flux, (**b**) downward shortwave radiation, and (**c**) latent heat flux. Positive values follow the sign conventions stated in each panel. All flux anomalies are in W m$^{-2}$. Event-level mixed-layer budget estimates and uncertainty are reported in the text and Supplementary Table S9.

#### 4.2.3. Upper-Ocean Currents and Makassar Transport

Current differences at the surface and the native level nearest 100 m (97.04 m) show distinct upper-ocean circulation patterns between the two event groups (Figure 6). Direct ORAS5 integration across the fixed Makassar section yields upper-300-m transport of −10.02 Sv for EP events and −10.40 Sv for CP events. The EP-minus-CP difference is +0.38 Sv with a 95% interval of $[-0.33, 1.09]$ Sv. Full-depth values are −11.76 and −12.26 Sv,

giving a difference of +0.50 Sv with a 95% interval of $[-0.47, 1.48]$ Sv. The transport-core depths are 135.9 m in EP events and 133.1 m in CP events; the difference is +2.9 m with a 95% interval of $[0.0, 8.6]$ m. Heat transport is −0.826 PW for EP and −0.877 PW for CP, with a difference of +0.051 PW and a 95% interval of $[-0.026, 0.123]$ PW. Exact two-sided permutation $p$-values for these four differences, in the same order, are $p = 0.365, 0.397, 1.000$, and 0.254, respectively. The volume- and heat-transport point estimates suggest slightly weaker southward transport during EP events, while the core-depth estimate provides no resolved shoaling. With five events per group, these contrasts remain unresolved.




Shading: $\Delta u = u_{EP} - u_{CP}$ (eastward positive). ⟶ 0.05 m s$^{-1}$; identical vector scale in both panels.

**Figure 6.** ORAS5 EP-minus-CP current differences at (**a**) the surface and (**b**) the native level nearest 100 m (97.04 m), based on five 1 July–30 June event windows per flavor. Shading provides the eastward-velocity difference $\Delta u = u_{EP} - u_{CP}$ in m s$^{-1}$, with positive values indicating a more eastward velocity or a weaker westward velocity during EP events. Black arrows show the corresponding horizontal vector difference $(\Delta u, \Delta v)$; the reference vector is 0.05 m s$^{-1}$, and both panels use the same scale. Makassar section volume transport, heat transport, and transport-core depth are reported in the text and Supplementary Table S8.

### *4.3. Modeled Coral Habitat Suitability*

The initial predictor screen identifies strong correlations between mean SST and SST variability ($\rho = 0.72$–$0.76$ across folds) and between nitrate and phosphate ($\rho = 0.75$–$0.82$). Screening was repeated inside each training fold before model fitting. The earlier random-split AUC is 0.912. Under ten repetitions of five-fold spatial-block validation, the full model yields an AUC of 0.845 with a 95% interval of $[0.814, 0.876]$, TSS 0.56 with a 95% interval of $[0.49, 0.63]$, and Boyce index 0.70 with a 95% interval of $[0.61, 0.78]$. Applying 30-km thinning leaves 617 occurrences and yields an AUC of 0.833 with a 95% interval of $[0.801, 0.864]$, TSS 0.54, and Boyce index 0.67. The decline from the random split quantifies the optimism caused by spatially neighboring training and test records.

Removing the SST block under the same spatial folds lowers AUC from 0.845 to 0.811, TSS from 0.56 to 0.49, and Boyce index from 0.70 to 0.62. The paired AUC change is −0.034, with a fold-bootstrap 95% interval of $[-0.058, -0.012]$ and paired $p < 0.05$. SST therefore carries measurable predictive information after bathymetric and biogeochemical screening. The EP and CP scenarios still yield different modeled suitability in the Java Sea, west of Sumatra, south of Java, and the Banda–Halmahera region; these maps describe suitability under the fitted model (Figure 7).

### *4.4. Reproducible Checks and Status of Confirmatory Analyses*

The prespecified classification was reproduced independently from NOAA PSL monthly ERSSTv5 Niño-3, Niño-4, and Niño-3.4 anomalies. The dominance rule reproduces all ten labels (Table 3). The 0.3 °C margin retains the five EP events and classifies 1994/95, 2002/03, 2006/07, and 2009/10 as mixed, leaving 2004/05 as the sole CP event. The Freund et al. decision tree provides three EP and seven CP events. Under this sensitivity, EP-minus-CP differences are 37.09 MHW days and 54.05 °C·days of cumulative intensity. Significant-area field tests remain nonsignificant, maximum-statistic field tests

yield $p = 0.050$ and 0.025, and the corresponding FDR areas are 0.056% and 0.039%. Across the ten candidate events, the continuous $D = N_3 - N_4$ association with domain-mean cumulative intensity remains uncertain ($r = 0.316$, $p = 0.374$).

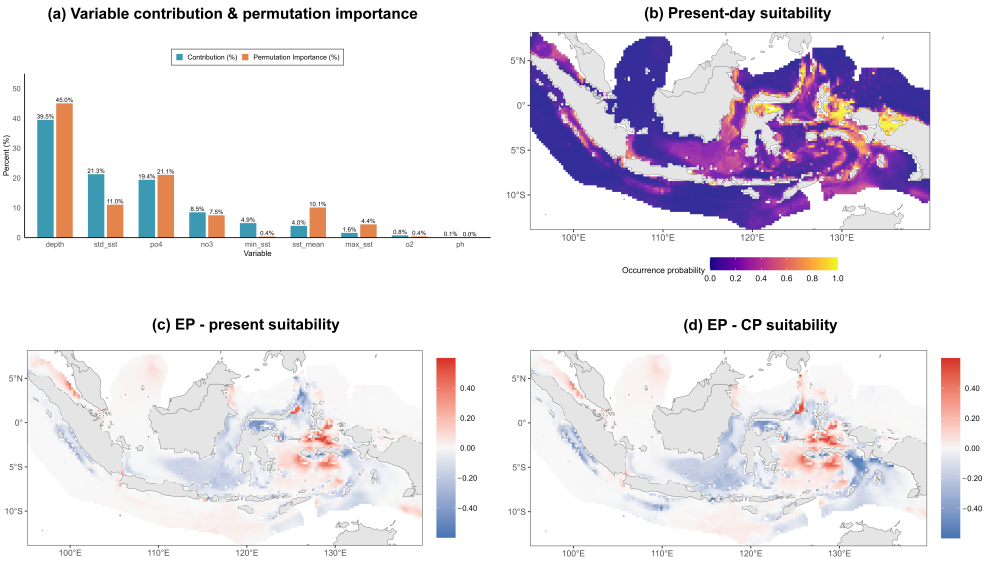



**Figure 7.** MaxEnt habitat-suitability outputs. (**a**) Heuristic variable contribution and permutation importance from the random-split model. (**b**) Baseline Scleractinia suitability. (**c**) EP-minus-baseline suitability. (**d**) EP-minus-CP suitability. The maps represent modeled environmental suitability. The "occurrence probability" scale displayed in panel (**b**) is the model's cloglog output and is interpreted here as relative environmental suitability, not observed coral occurrence. Spatial-block validation and the 30-km thinning sensitivity are reported in the text and Supplementary Table S10.

The OISST rerun covers all 14,975 calendar days from 1 January 1982 through 31 December 2022 on 17,725 valid ocean cells. Every annual file passed coordinate, date-count, and completeness checks. The fixed-baseline MHW fields, five sensitivity configurations, event-level EP/CP arrays, exact spatial tests, detrended EOFs, annual lag tests, seasonal coverage, and raw and climate-index-adjusted trends were recomputed from this daily record. Figures 2–4 and Supplementary Tables S2–S6 and S11 and Figures S1–S5 report these completed results.

The revised analyses now include the annual association-model summary, direct Makassar volume and heat transport, a mixed-layer heat-budget decomposition, and repeated spatial-block MaxEnt validation. The official WPPNRI snapshot has been acquired and audited for source fields and study-domain overlap. FMA results are reported as polygon-based exposure summaries; an operational composite ranking would additionally require a prespecified decision rule that combines exposure, habitat suitability, and their uncertainties.

The official polygons contain 7912 valid OISST cell centers. WPPNRI 571, 572, 717, and 718 have study-domain coverage of 97.5%, 80.0%, 92.0%, and 97.1%, respectively; the other seven polygons are fully contained. WPPNRI 711 has the largest EP-minus-CP point estimate at 34.25 MHW days, with a 95% event-bootstrap interval of $[-11.08, 86.41]$ and exact $p = 0.262$. Every FMA interval spans zero, and every exact $p$-value exceeds 0.25 (Supplementary Table S12). The official-polygon results therefore provide descriptive management-unit exposure without a stable ENSO-flavor ranking.

## 5. Discussion

### *5.1. Methodological Contribution Relative to Previous Work*

Previous Indonesian studies established regional MHW variability, climate-mode associations, surface heat-flux structure, advection, and south-Java upwelling [11–13]. Their analyses did not report an archipelago-wide EP/CP comparison with an explicit event list, classification-boundary audit, event-level uncertainty, and spatial field control in the same design. The present analysis fills that methodological gap. The literature comparison in Table 1 also clarifies that the MHW detector and MaxEnt model are established methods. The contribution lies in the ENSO-flavor sampling and inference design, joined here with section-integrated ITF diagnostics, a mixed-layer budget with an explicit residual, and spatially separated habitat validation on the same event window.

The completed MHW analysis treats the ten ENSO events as the independent units. It combines Hedges' $g$, 10,000 within-flavor bootstrap samples, FDR control, and all 252 possible five-versus-five label allocations. The result changes the evidentiary status of the central flavor comparison: EP MHW point estimates exceed CP MHW estimates, while the event-level intervals cross zero and the field tests remain nonsignificant. The 0.3 °C classification audit further shows that four nominal CP events lie near the flavor boundary. Reporting the continuous $D$ result alongside the binary composite makes this instability visible.

The long-term analysis supplies the strongest quantitative result. The area-weighted trend is 11.37 MHW days per decade, 90.5% of the domain passes FDR control, and both field tests give $p = 0.001$. Removing fitted Niño-3.4 and DMI variability leaves 95.2% of the domain FDR significant. The annual EOF and lag analysis also resolves the temporal mismatch raised during review, with a concurrent PC1 relation and no corrected evidence for delayed one- to three-year responses.

The added experiments sharpen the interpretation. The full annual association model raises the adjusted explained fraction from 0.23 to 0.44 and lowers leave-one-year-out RMSE by 18.8%. VIF and residual diagnostics do not indicate severe collinearity, autocorrelation, heteroscedasticity, or non-normality. Two years exceed the Cook's distance screening threshold, so the regression remains an association model. Makassar volume transport, heat transport, transport-core depth, and each mixed-layer budget term have confidence intervals that include zero. The physical diagnostics therefore provide event-level estimates with explicit uncertainty. Surface forcing provides the largest positive resolved budget difference, but the opposing residual is substantial and prevents single-process attribution. Spatial-block MaxEnt validation lowers AUC from the random-split value of 0.912 to 0.845. SST-block removal produces a further paired decline of 0.034, which identifies transferable predictive information associated with the thermal variables. Table 4 summarizes the evidence supporting each physical and ecological interpretation.

**Table 4.** Observed or modeled EP/CP contrasts and the diagnostic required for each physical or ecological interpretation.

| Process | EP El Niño State | CP El Niño State | Implication for MHW Risk |
|---|---|---|---|
| Surface forcing | Positive net and shortwave heat-flux anomalies occur in parts of the southern corridor; the budget difference is $+0.203$ °C month$^{-1}$. | The corresponding surface contribution is smaller. | The surface interval $[-0.167, 0.606]$ includes zero and the closure residual is $-0.149$ °C month$^{-1}$. |

**Table 4.** *Cont.*

| Process | EP El Niño State | CP El Niño State | Implication for MHW Risk |
|---|---|---|---|
| Ocean circulation | Makassar volume and heat transports are slightly weaker in the point estimates; the core-depth contrast is negligible. | Southward volume and heat transports are larger in magnitude. | The transport intervals include zero, so the EP–CP difference remains unresolved. |
| Habitat suitability | The fitted environmental scenario changes modeled suitability in several southern areas. | The fitted CP scenario produces a different suitability pattern. | Spatial-block AUC is 0.845; SST removal lowers it by 0.034, while ecological impacts still require field observations. |

### *5.2. Strengths of the Multi-Source Approach*

The main strength is the common domain and event window used across data types. The OISST record supplies complete daily surface coverage over 41 years, and the fixed early baseline preserves the later rise in threshold exceedance. MHW metrics, surface-flux fields, currents, environmental predictors, and management boundaries can therefore be compared at matched locations. Each source retains a limited interpretation: OISST describes surface thermal extremes, reanalysis fields describe physical covariation, MaxEnt estimates environmental suitability, and official FMA polygons summarize validated gridded quantities. Related work in other data-intensive fields has examined robust anomaly detection, interpretability, and risk assessment in complex systems [50–54].

The EP composite has larger domain-mean MHW-day and cumulative-intensity estimates than the CP composite, and the largest positive map differences occur along parts of the south Java–Sumatra margin. With negative values denoting southward flow, the ORAS5 section analysis places the corresponding Makassar difference at $+0.38$ Sv in the upper 300 m and $+0.50$ Sv over the full depth. The mixed-layer budget partitions the $+0.024$ °C month$^{-1}$ EP-minus-CP tendency into $+0.203$ from surface forcing, $-0.038$ from horizontal advection, $+0.008$ from entrainment, and $-0.149$ from the residual, all in °C month$^{-1}$. The intervals include zero, and the opposing residual is substantial, so these terms leave the process attribution tentative.

### *5.3. Ocean-Science Interpretation and Marine-Risk Management Relevance*

The South Java–Sumatra margin contains several of the largest positive EP-minus-CP MHW estimates and remains a useful monitoring region. The exact field tests show that this flavor contrast is not spatially significant at the 0.05 level. Long-term exposure supplies firmer guidance because the positive trend is widespread, FDR controlled, and stable after the two climate-index adjustments. Published ITF studies indicate that the physical response can vary by section and depth [7–10].

The present sample does not support an operational FMA ranking by ENSO flavor. The official WPPNRI polygons now support descriptive zone summaries, while an operational combined rank still requires gridded out-of-fold habitat predictions, rank-stability tests, and a stable flavor effect in a larger event set. The spatial-block AUC of 0.845, with a 95% interval of $[0.814, 0.876]$, supports environmental-suitability screening within the sampled region. The 30-km thinning sensitivity gives AUC 0.833 $[0.801, 0.864]$. Coral cover, bleaching, and mortality observations are still required to assess realized ecological impact.

### *5.4. Limitations*

Five events per flavor provide limited power, and four of the five CP labels become mixed under the 0.3 °C separation rule. The event-bootstrap intervals and field tests confirm this sampling limitation. The climate-index-adjusted trend analysis removes linear Niño-3.4 and DMI variability; it does not constitute formal detection and attribution. Confidence intervals for Makassar transport, heat transport, transport-core depth, and mixed-layer budget terms include zero. The mixed-layer residual is large enough to preclude attribution to one resolved process. The 41-year OLS models remain associational, despite the improved adjusted $R^2$ and leave-one-year-out RMSE. Spatial blocking lowers MaxEnt performance relative to random splitting, and correlated SST and nutrient predictors complicate single-variable interpretation. Modeled suitability does not measure bleaching or mortality. ERA5 has shared observational ancestry with OISST. The official polygons support descriptive FMA exposure estimates, while an operational composite rank would require a prespecified decision rule and propagation of exposure and habitat-model uncertainty.

The official WPPNRI geometry has been acquired, although an operational combined ranking still requires saved gridded out-of-fold habitat predictions and a rank-stability analysis.

## 6. Conclusions

The fixed-baseline OISST analysis shows a large and spatially extensive rise in Indonesian MHW exposure from 1982 to 2022. Annual MHW days increase by an area-weighted 11.37 days per decade, and 90.5% of the domain passes FDR control. The increase remains widespread after linear Niño-3.4 and DMI adjustment. Detrended EOF analysis identifies a concurrent basin-scale relation with DJF Niño-3.4.

The five EP windows have greater mean MHW exposure than the five CP windows, while the event-bootstrap intervals cross zero, the exact domain-mean permutation tests are nonsignificant, and no cell passes FDR control for MHW days or cumulative intensity. Classification sensitivity and the continuous flavor analysis show that this event-scale contrast remains uncertain. The annual association model gains explanatory and out-of-sample predictive performance when heat-flux and current covariates are included. ORAS5 point estimates give slightly weaker southward EP volume and heat transport and a positive mixed-layer tendency; their intervals include zero, and the large mixed-layer residual limits process attribution. Spatial-block validation supports useful habitat-model prediction within the sampled region, and the SST-block ablation identifies transferable information in the thermal predictors. The long-term MHW increase remains the principal result; interpretations of the physical and ecological pathways remain tentative because they are based on a small event sample and correlative models.

**Supplementary Materials:** The following supporting information can be downloaded at https://www.mdpi.com/article/10.3390/rs18203555/s1, Figure S1: Leading EOFs of grid-cell-detrended annual MHW days and their standardized PCs; Figure S2: Monthly climatology of daily MHW areal coverage for 1982–2022; Figure S3: Pearson correlation between detrended annual MHW days and detrended annual Niño-3.4; Figure S4: Correlations between the first three detrended PCs and DJF Niño-3.4 at PC lags of zero to three years; Figure S5: Theil–Sen trends in annual MHW days for 1982–2022 before and after linear annual Niño-3.4 and DMI adjustment; Table S1: Input provenance for the completed analyses; Table S2: Reproduced ENSO classification; Table S3: Detection sensitivity relative to the primary definition; Table S4: Domain-level EP and CP estimates with event-level inference; Table S5: Grid-cell multiplicity control and exact field significance; Table S6: Concurrent PC1 relations; Table S7: Association-model performance, coefficients, and diagnostics; Table S8: Makassar Strait diagnostics for five EP and five CP event windows; Table S9: EP-minus-CP mixed-layer heat-budget terms; Table S10: GBIF record flow, spatial validation, thinning sensitivity, and grouped SST ablation;

Table S11: Theil–Sen and Mann–Kendall trend results for annual MHW days; Table S12: Official-polygon WPPNRI summaries of event-window MHW days.

**Author Contributions:** Conceptualization, Q.X. and Z.J.; methodology, Q.X. and J.Z.; validation, Q.X., J.Z., and L.L.; formal analysis, Q.X. and Z.J.; investigation, J.Z. and Z.J.; resources, Q.X.; data curation, Z.J. and L.L.; writing, original draft preparation, Q.X. and J.Z.; writing, review and editing, all authors; visualization, J.Z. and Z.J.; supervision, Q.X.; project administration, Q.X. All authors have read and agreed to the published version of the manuscript.

**Funding:** This research was funded by the Humanities and Social Sciences Project of the Department of Education of Anhui Province (Grant No. 2024AH052995) and the Key Project of Philosophy and Social Sciences in Universities of Anhui Province (Grant No. 2024AH052968).

**Institutional Review Board Statement:** Not applicable.

**Informed Consent Statement:** Not applicable.

**Data Availability Statement:** The completed MHW analyses use NOAA OISST v2.1, available at https://doi.org/10.25921/RE9P-PT57 (accessed on 9 September 2026), and NOAA PSL ERSSTv5 Niño indices, available from https://psl.noaa.gov/gcos_wgsp/Timeseries/ (accessed on 9 September 2026). The author archive of OISST was obtained on 1 February 2025 and the revision subset used for the completed rerun was retrieved on 9 September 2026. NOAA ONI v5 was obtained on 12 April 2025, and the ERSSTv5 Niño-region series used for the classification audit were retrieved on 9 September 2026. The DMI series was obtained from the NOAA PSL HadISST dipole-mode-index record. The GBIF occurrence archive was retrieved on 20 April 2026 and is available at https://doi.org/10.15468/dl.td23by (accessed on 20 April 2026); Scleractinia taxon key 714 defines the order-level subset used in the habitat model. Persistent product records and retrieval dates are ERA5 single levels https://doi.org/10.24381/cds.adbb2d47 (accessed on 3 February 2025), ERA5 monthly pressure levels https://doi.org/10.24381/cds.6860a573 (accessed on 18 March 2025), ETOPO 2022 https://doi.org/10.25921/fd45-gt74 (accessed on 4 February 2025), ECMWF ORAS5 https://doi.org/10.24381/cds.67e8eeb7 (accessed on 20 September 2026) (physical-diagnostic subset) , Copernicus Marine biogeochemistry https://doi.org/10.48670/moi-00019 (accessed on 21 August 2025), and NCEP/DOE R2 https://doi.org/10.5065/KVQZ-YJ93 (accessed on 7 May 2026). The KKP WPPNRI portal was accessed on 7 March 2026. The official polygon geometry used in Figure 1 and the FMA calculations is BIG MapServer layer 21, available from https://kspservices.big.go.id/satupeta/rest/services/PUBLIK/SUMBER_DAYA_ALAM_DAN_LINGKUNGAN/MapServer/21 (accessed on 13 September 2026); its archived snapshot was retrieved on 13 September 2026.

**Acknowledgments:** The authors would like to acknowledge the technical support from the College of Oceanic and Atmospheric Sciences, Ocean University of China, Qingdao.

**Conflicts of Interest:** The authors declare no conflicts of interest.

## Abbreviations

| | |
|---|---|
| AUC | area under the receiver operating characteristic curve |
| CI | confidence interval |
| CP | Central-Pacific El Niño |
| DMI | dipole mode index |
| DJF | December–February |
| ECMWF | European Centre for Medium-Range Weather Forecasts |
| ENSO | El Niño–Southern Oscillation |
| EOF | empirical orthogonal function |
| EP | Eastern-Pacific El Niño |
| FDR | false discovery rate |
| FMA | Fisheries Management Area |

| | |
|---|---|
| GBIF | Global Biodiversity Information Facility |
| HAC | heteroscedasticity- and autocorrelation-consistent |
| HC3 | heteroscedasticity-consistent type 3 |
| ICDC | Integrated Climate Data Center |
| ITF | Indonesian Throughflow |
| LM | Lagrange multiplier |
| MHW | marine heatwave |
| MK | Mann–Kendall |
| OISST | Optimum Interpolation Sea Surface Temperature |
| OLS | ordinary least squares |
| ONI | Oceanic Niño Index |
| ORAS5 | Ocean ReAnalysis System 5 |
| PC | principal component |
| RMSE | root-mean-square error |
| SON | September–November |
| SST | sea surface temperature |
| TSS | true skill statistic |
| VIF | variance-inflation factor |
| WPPNRI | Indonesian Fisheries Management Areas |

## References


1. Hobday, A.J.; Alexander, L.V.; Perkins, S.E.; Smale, D.A.; Straub, S.C.; Oliver, E.C.; Benthuysen, J.A.; Burrows, M.T.; Donat, M.G.; Feng, M.; et al. A hierarchical approach to defining marine heatwaves. *Prog. Oceanogr.* **2016**, *141*, 227–238. [CrossRef]
2. Oliver, E.C.; Benthuysen, J.A.; Darmaraki, S.; Donat, M.G.; Hobday, A.J.; Holbrook, N.J.; Schlegel, R.W.; Sen Gupta, A. Marine Heatwaves. *Annu. Rev. Mar. Sci.* **2021**, *13*, 313–342. [CrossRef]
3. Huang, B.; Liu, C.; Banzon, V.; Freeman, E.; Graham, G.; Hankins, B.; Smith, T.; Zhang, H.M. Improvements of the Daily Optimum Interpolation Sea Surface Temperature (DOISST) Version 2.1. *J. Clim.* **2021**, *34*, 2923–2939. [CrossRef]
4. National Centers for Environmental Information. NOAA 0.25-Degree Daily Optimum Interpolation Sea Surface Temperature (OISST), Version 2.1. 2020. Author Archive Obtained 1 February 2025. Available online: https://www.ncei.noaa.gov/metadata/geoportal/rest/metadata/item/gov.noaa.ncdc:C01606/html (accessed on 9 September 2026).
5. Sprintall, J.; Gordon, A.L.; Koch-Larrouy, A.; Lee, T.; Potemra, J.T.; Pujiana, K.; Wijffels, S.E. The Indonesian seas and their role in the coupled ocean–climate system. *Nat. Geosci.* **2014**, *7*, 487–492. [CrossRef]
6. Veron, J.; Devantier, L.M.; Turak, E.; Green, A.L.; Kininmonth, S.; Stafford-Smith, M.; Peterson, N. Delineating the Coral Triangle. *Galaxea J. Coral Reef Stud.* **2009**, *11*, 91–100. [CrossRef]
7. Gordon, A.L.; Napitu, A.; Huber, B.A.; Gruenburg, L.K.; Pujiana, K.; Agustiadi, T.; Kuswardani, A.; Mbay, N.; Setiawan, A. Makassar Strait Throughflow Seasonal and Interannual Variability: An Overview. *J. Geophys. Res. Ocean* **2019**, *124*, 3724–3736. [CrossRef]
8. Li, M.; Gordon, A.L.; Gruenburg, L.K.; Wei, J.; Yang, S. Interannual to Decadal Response of the Indonesian Throughflow Vertical Profile to Indo-Pacific Forcing. *Geophys. Res. Lett.* **2020**, *47*, e2020GL087679. [CrossRef]
9. Xu, W.; Yuan, D.; Li, M. Interannual Variability of the Indonesian Throughflow in the Makassar Strait Associated With the 2015/2016 Super El Niño. *Geophys. Res. Lett.* **2025**, *52*, e2024GL111709. [CrossRef]
10. Jin, H.; Li, M.; Wang, D.; Xin, S.; Gordon, A.L.; Gruenburg, L.K. Changes of the Indonesian Throughflow Spreading in the Indian Ocean During Extreme Indian Ocean Dipole Events. *J. Geophys. Res. Oceans* **2026**, *131*, e2026JC023998. [CrossRef]
11. Iskandar, M.R.; Ismail, M.F.A.; Arifin, T.; Chandra, H. Marine heatwaves of sea surface temperature off south Java. *Heliyon* **2021**, *7*, e08618. [CrossRef]
12. Beliyana, E.; Ningsih, N.S.; Gunawan, S.R.; Tarya, A. Characteristics of Marine Heatwaves in the Indonesian Waters during the PDO, ENSO, and IOD Phases and Their Relationships to Net Surface Heat Flux. *Atmosphere* **2023**, *14*, 1035. [CrossRef]
13. Ningsih, N.S.; Beliyana, E.; Kamila, I.H.; Tarya, A. Long-term characteristics of marine heatwaves (1982–2021) in Indonesian water and their impact on upwelling (case study: Southern Java). *Front. Mar. Sci.* **2025**, *12*, 1504995. [CrossRef]
14. Lyu, Y.; Xiao, F.; Lu, M.; Wang, D.; Wu, Q.; Wang, P.; Zeng, Y. Increased Frequency but Decreased Intensity of Marine Heatwaves Around Coral Reef Regions in the Southern South China Sea. *J. Geophys. Res. Oceans* **2024**, *129*, e2024JC021235. [CrossRef]
15. Yao, Y.; Wang, C. Subsurface Marine Heatwaves in the South China Sea. *J. Geophys. Res. Oceans* **2024**, *129*, e2024JC021356. [CrossRef]

16. Zhang, N.; Lan, J.; Dong, C. Subsurface Heatwaves and Cold Spells in the South China Sea Regulated by ENSO: Role of the South China Sea Throughflow. *Geophys. Res. Lett.* **2025**, *52*, e2025GL114692. [CrossRef]
17. Lu, X.; Xiao, F.; Wu, Z.; Huang, J.; Wang, Q.; Wang, D. A Weakened East Asian Winter Monsoon Triggered Record-Breaking Marine Heatwaves in the South China Sea During 2023–2024. *J. Geophys. Res. Oceans* **2026**, *131*, e2026JC024234. [CrossRef]
18. Kao, H.Y.; Yu, J.Y. Contrasting Eastern-Pacific and Central-Pacific Types of ENSO. *J. Clim.* **2009**, *22*, 615–632. [CrossRef]
19. Kug, J.S.; Jin, F.F.; An, S.I. Two Types of El Niño Events: Cold Tongue El Niño and Warm Pool El Niño. *J. Clim.* **2009**, *22*, 1499–1515. [CrossRef]
20. Capotondi, A.; Wittenberg, A.T.; Newman, M.; Di Lorenzo, E.; Yu, J.Y.; Braconnot, P.; Cole, J.; Dewitte, B.; Giese, B.; Guilyardi, E.; et al. Understanding ENSO Diversity. *Bull. Am. Meteorol. Soc.* **2015**, *96*, 921–938. [CrossRef]
21. Timmermann, A.; An, S.I.; Kug, J.S.; Jin, F.F.; Cai, W.; Capotondi, A.; Cobb, K.M.; Lengaigne, M.; McPhaden, M.J.; Stuecker, M.F.; et al. El Niño–Southern Oscillation complexity. *Nature* **2018**, *559*, 535–545. . Correction in *Nature* **2019**, *567*, E3. [CrossRef]
22. Skirving, W.; Marsh, B.; De La Cour, J.; Liu, G.; Harris, A.; Maturi, E.; Geiger, E.; Eakin, C.M. CoralTemp and the Coral Reef Watch Coral Bleaching Heat Stress Product Suite Version 3.1. *Remote Sens.* **2020**, *12*, 3856. [CrossRef]
23. Freeman, L.A.; Kleypas, J.A.; Miller, A.J. Coral Reef Habitat Response to Climate Change Scenarios. *PLoS ONE* **2013**, *8*, e82404. [CrossRef]
24. Januar, H.I.; Hidayah, I.; Humaida, N.; Salnuddin; Iswani, S.; Hidayat, A. Habitat Suitability Modeling of *Acropora* spp. Distribution in Coral Triangle Area of Maluku Waters, Indonesia under Influence of Future Climate Change and Coastal Pollution. *Agric. Nat. Resour.* **2023**, *57*, 869–876. [CrossRef]
25. Couce, E.; Ridgwell, A.; Hendy, E.J. Future habitat suitability for coral reef ecosystems under global warming and ocean acidification. *Glob. Change Biol.* **2013**, *19*, 3592–3606. [CrossRef]
26. Hobday, A.; Oliver, E.; Sen Gupta, A.; Benthuysen, J.; Burrows, M.; Donat, M.; Holbrook, N.; Moore, P.; Thomsen, M.; Wernberg, T.; et al. Categorizing and Naming Marine Heatwaves. *Oceanography* **2018**, *31*, 162–173. [CrossRef]
27. Oliver, E.C.J.; Donat, M.G.; Burrows, M.T.; Moore, P.J.; Smale, D.A.; Alexander, L.V.; Benthuysen, J.A.; Feng, M.; Sen Gupta, A.; Hobday, A.J.; et al. Longer and more frequent marine heatwaves over the past century. *Nat. Commun.* **2018**, *9*, 1324. [CrossRef]
28. Holbrook, N.J.; Scannell, H.A.; Sen Gupta, A.; Benthuysen, J.A.; Feng, M.; Oliver, E.C.J.; Alexander, L.V.; Burrows, M.T.; Donat, M.G.; Hobday, A.J.; et al. A global assessment of marine heatwaves and their drivers. *Nat. Commun.* **2019**, *10*, 2624. [CrossRef]
29. Liu, B.; Foo, S.A.; Guan, L. Optimization of thermal stress thresholds on regional coral bleaching monitoring by satellite measurements of sea surface temperature. *Front. Mar. Sci.* **2024**, *11*, 1438087. [CrossRef]
30. Phillips, S.J.; Anderson, R.P.; Schapire, R.E. Maximum entropy modeling of species geographic distributions. *Ecol. Model.* **2006**, *190*, 231–259. [CrossRef]
31. da Silveira, C.B.L.; Strenzel, G.M.R.; Maida, M.; Gaspar, A.L.B.; Ferreira, B.P. Coral Reef Mapping with Remote Sensing and Machine Learning: A Nurture and Nature Analysis in Marine Protected Areas. *Remote Sens.* **2021**, *13*, 2907. [CrossRef]
32. Roberts, D.R.; Bahn, V.; Ciuti, S.; Boyce, M.S.; Elith, J.; Guillera-Arroita, G.; Hauenstein, S.; Lahoz-Monfort, J.J.; Schröder, B.; Thuiller, W.; et al. Cross-validation strategies for data with temporal, spatial, hierarchical, or phylogenetic structure. *Ecography* **2017**, *40*, 913–929. [CrossRef]
33. Valavi, R.; Elith, J.; Lahoz-Monfort, J.J.; Guillera-Arroita, G. blockCV: An R Package for Generating Spatially or Environmentally Separated Folds for *k*-Fold Cross-Validation of Species Distribution Models. *Methods Ecol. Evol.* **2019**, *10*, 225–232. [CrossRef]
34. Dormann, C.F.; Elith, J.; Bacher, S.; Buchmann, C.; Carl, G.; Carré, G.; Marquéz, J.R.G.; Gruber, B.; Lafourcade, B.; Leitão, P.J.; et al. Collinearity: A review of methods to deal with it and a simulation study evaluating their performance. *Ecography* **2012**, *36*, 27–46. [CrossRef]
35. Badan Informasi Geospasial Republik Indonesia. Peta Wilayah Pengelolaan Perikanan RI, 2026. Government ArcGIS Polygon Service, Layer 21. Available online: https://kspservices.big.go.id/satupeta/rest/services/PUBLIK/SUMBER_DAYA_ALAM_DAN_LINGKUNGAN/MapServer/21 (accessed on 13 September 2026).
36. Kementerian Kelautan dan Perikanan Republik Indonesia. Peraturan Menteri Kelautan dan Perikanan Nomor 18/PERMEN-KP/2014 Tentang Wilayah Pengelolaan Perikanan Negara Republik Indonesia, 2014. Available online: https://jdih.kkp.go.id/Homedev/DetailPeraturan/486 (accessed on 13 September 2026).
37. NOAA National Centers for Environmental Information. ETOPO 2022 15 Arc-Second Global Relief Model. 2022. Available online: https://data.noaa.gov/metaview/page?xml=NOAA/NESDIS/NGDC/MGG/DEM//iso/xml/etopo_2022.xml&view=getDataView&header=none (accessed on 4 February 2025).
38. National Centers for Environmental Prediction. NCEP/DOE Reanalysis 2 (R2). NSF National Center for Atmospheric Research, Dataset d091000. 2000. Available online: https://gdex.ucar.edu/datasets/d091000/ (accessed on 7 May 2026).
39. Copernicus Climate Change Service. ERA5 Monthly Averaged Data on Pressure Levels from 1940 to Present. 2018. Available online: https://cds.climate.copernicus.eu/datasets/reanalysis-era5-pressure-levels-monthly-means?tab=overview (accessed on 18 March 2025).

40. Copernicus Climate Change Service. ORAS5 Global Ocean Reanalysis Monthly Data from 1958 to Present. 2021. Available online: https://cds.climate.copernicus.eu/datasets/reanalysis-oras5?tab=overview (accessed on 20 September 2026).
41. Zuo, H.; Balmaseda, M.A.; Tietsche, S.; Mogensen, K.; Mayer, M. The ECMWF Operational Ensemble Reanalysis–Analysis System for Ocean and Sea Ice: A Description of the System and Assessment. *Ocean Sci.* **2019**, *15*, 779–808. [CrossRef]
42. E.U. Copernicus Marine Service Information. Global Ocean Biogeochemistry Hindcast. 2018. Product GLOBAL_MULTIYEAR_BGC_001_029. Available online: https://data.marine.copernicus.eu/product/GLOBAL_MULTIYEAR_BGC_001_029/description (accessed on 21 August 2025).
43. Freund, M.B.; Henley, B.J.; Karoly, D.J.; McGregor, H.V.; Abram, N.J.; Dommenget, D. Higher Frequency of Central Pacific El Niño Events in Recent Decades Relative to Past Centuries. *Nat. Geosci.* **2019**, *12*, 450–455. [CrossRef]
44. Benjamini, Y.; Hochberg, Y. Controlling the False Discovery Rate: A Practical and Powerful Approach to Multiple Testing. *J. R. Stat. Soc. Ser. B Stat. Methodol.* **1995**, *57*, 289–300. [CrossRef]
45. Wilks, D.S. "The Stippling Shows Statistically Significant Grid Points": How Research Results are Routinely Overstated and Overinterpreted, and What to Do about It. *Bull. Am. Meteorol. Soc.* **2016**, *97*, 2263–2273. [CrossRef]
46. GBIF.org. GBIF Occurrence Download. 2026. Download Key 0033412-260409193756587. Available online: (accessed on 20 April 2026). [CrossRef]
47. Allouche, O.; Tsoar, A.; Kadmon, R. Assessing the accuracy of species distribution models: Prevalence, kappa and the true skill statistic (TSS). *J. Appl. Ecol.* **2006**, *43*, 1223–1232. [CrossRef]
48. Boyce, M.S.; Vernier, P.R.; Nielsen, S.E.; Schmiegelow, F.K. Evaluating resource selection functions. *Ecol. Model.* **2002**, *157*, 281–300. [CrossRef]
49. Susanto, R.D.; Ffield, A.; Gordon, A.L.; Adi, T.R. Variability of Indonesian throughflow within Makassar Strait, 2004–2009. *J. Geophys. Res. Oceans* **2012**, *117*, C09013. [CrossRef]
50. Huang, X.; Xiao, H.; Zeng, Z.; Qiu, Z.; Zhu, W.; Zhang, S.; Xiao, R. Toward Robust Anomaly Detection in Noisy Time Series via Diffusion-Driven Denoising and Disentanglement. *J. Supercomput.* **2026**, *82*, 250. [CrossRef]
51. Shao, W. Policy-Driven Vulnerability Risk Quantification Framework for Large-Scale Cloud Infrastructure Data Security. In *Proceedings of the 2026 5th International Conference on Cyber Security*; Artificial Intelligence and Digital Economy: New York, NY, USA, 2026; pp. 40–45. [CrossRef]
52. Shao, W. Interpretable Ensemble Learning for Network Traffic Anomaly Detection: A SHAP-Based Explainable AI Framework for Embedded Systems Security. In Proceedings of the 2026 14th International Symposium on Digital Forensics and Security, Boston, MA, USA, 19–20 March 2026; pp. 1–4. [CrossRef]
53. Shao, W. Design and Implementation of an Open-Source Security Framework for Cloud Infrastructure. In Proceedings of the 2026 12th International Symposium on System Security, Safety, and Reliability, Xiangyang, China, 16–17 May 2026; pp. 53–60. [CrossRef]
54. Shao, W. Continuous Trust in Multi-Cloud Environments: An Evidence-Driven Security Assurance Method. In Proceedings of the 2026 2nd International Conference on Emerging and Intelligent Technologies and Systems, Valencia, Spain, 9–12 June 2026; pp. 123–128. [CrossRef]


**Disclaimer/Publisher's Note:** The statements, opinions and data contained in all publications are solely those of the individual author(s) and contributor(s) and not of MDPI and/or the editor(s). MDPI and/or the editor(s) disclaim responsibility for any injury to people or property resulting from any ideas, methods, instructions or products referred to in the content.